

Skin-Integrated Graphene-Embedded Lead Zirconate Titanate Rubber for Energy Harvesting and Mechanical Sensing

Yiming Liu, Ling Zhao, Lingyun Wang, Huanxi Zheng, Dengfeng Li, Raudel Avila, King W. C. Lai, Zuankai Wang, Zhaoqian Xie,* Yunlong Zi,* and Xinge Yu*

Thin, soft, skin-like electronics capable of transforming body mechanical motions to electrical signals have broad potential applications in biosensing and energy harvesting. Forming piezoelectric materials into flexible and stretchable formats and integrating with soft substrate would be a considerable strategy for this aspect. Here, a skin-integrated rubbery electronic device that associates with a simple low-cost fabrication method for a ternary piezoelectric rubber composite of graphene, lead zirconate titanate (PZT), and polydimethylsiloxane (PDMS) is introduced. Comparing to the binary composite that blend with PZT and PDMS, the graphene-embedded ternary composite exhibits a significant enhancement of self-powered behavior, with a maximum power density of $972.43 \mu\text{W cm}^{-3}$ under human walking. Combined experimental and theoretical studies of the graphene-embedded PZT rubber allow the skin-integrated electronic device to exhibit excellent mechanical tolerance to bending, stretching, and twisting for thousands of cycles. Customized device geometries guided by optimized mechanical design enable a more comprehensive integration of the rubbery electronics with the human body. For instance, annulus-shape devices can perfectly mount on the joints and ensure great power output and stability under continuous and large deformations. This work demonstrates the potential of large-area, skin-integrated, self-powered electronics for energy harvesting as well as human health related mechanical sensing.

1. Introduction

Thin, soft skin-integrated electronics have attracted great attentions due to their advantages such as flexible, light-weight, and mechanical compatible with human body, thus offer unique capabilities in detecting vital information and continuous monitoring human health.^[1–8] Recent advances in materials development,^[9–15] electronics miniaturization,^[16–20] mechanics optimization,^[18,21–24] and system-level integration^[17,25–28] build up the foundations for flexible and stretchable electronics^[29–32] which are able to be integrated together with skin. Considering power supply for this new kind of soft electronics, conversion of mechanical energy from human body activities and motions to electricity is a considerable route.^[4,5,13,33,34] Various kinds of technologies, such as piezoelectric,^[35–40] triboelectric,^[41–47] electromagnetic,^[48] and pyroelectric^[49–51] have been considered and studied. Among these self-powered technologies, piezoelectric generators have proven to be a great candidate as energy harvesters

for skin-integrated or even biointegrated electronics, due to the combination of their excellent electrical properties and advanced mechanical designs.^[5,18,52,53] Materials and mechanical engineering in piezoelectric materials, including lead zirconate titanate (PZT),^[1,11,18,19,24,38] PVDF,^[20,21,53] BaTiO₃,^[36,52,54] NaNbO₃,^[15,55] and ZnO^[35,56] have been made great progress and realized outstanding electromechanical properties. However, complicated fabrication processes involving high temperature deposition, multiple steps photolithographs, physical/chemical etchings, and transfer printings are typically needed to meet the requirement of flexibility.^[17,18,57–59]


To realize rapid and low-cost processing techniques for soft piezoelectric based electronics, inherent flexibility of the materials should be carefully considered, as which affords the possibility for large-area fabrication relevant routes, such as screen-printing and roll to roll technologies.^[9] One promising method for realizing inherent flexible piezoelectric materials is designing polymer-matrix composites which typically consist of piezoelectric ceramic powders and silicone rubbers (polydimethylsiloxane, PDMS).^[11,15,60–63] This

Y. Liu, L. Zhao, Dr. L. Wang, Dr. D. Li, Dr. K. W. C. Lai, Dr. Z. Xie, Dr. X. Yu
Department of Biomedical Engineering
City University of Hong Kong
Hong Kong 999077, P. R. China
E-mail: zhaoqxie@cityu.edu.hk; xingeyu@cityu.edu.hk

Dr. L. Wang, Dr. Y. Zi
Department of Mechanical and Automation Engineering
Chinese University of Hong Kong
Hong Kong 999077, P. R. China
E-mail: ylzi@cuhk.edu.hk

H. Zheng, Prof. Z. Wang
Department of Mechanical Engineering
City University of Hong Kong
Hong Kong 999077, P. R. China

R. Avila
Department of Mechanical Engineering
McCormick School of Engineering
Northwestern University
Evanston, IL 60208, USA

 The ORCID identification number(s) for the author(s) of this article can be found under <https://doi.org/10.1002/admt.201900744>.

DOI: 10.1002/admt.201900744

kind of composite enables significant decrease of modulus from tens of GPa in pure piezoelectric ceramic to 10^2 – 10^4 kPa, and therefore enhance their stretchability.^[11,15,60] However, these reported composites are mostly utilized as strain sensors for mechanical sensing, rather than energy harvesters, which is due to the extremely high internal impedance and very limited current output.^[60] The conductivity of such composite ($\approx 10^{-9}$ S m⁻¹) is extremely low, even when the ratio of PZT is enhanced to 50%.^[60] Notably, the composite of PZT:PDMS = 50:50 is already very stiff, sacrificing its advantage of flexibility.^[60] Therefore, decreasing the internal impedance of the composite could effectively improve the piezoelectric properties, and thus provide the possibility for soft energy harvesters.^[64] We summarize the performances of the piezoelectric materials in energy harvesting as shown in Table S1 of the Supporting Information.

Here, we present a simple rubbery like piezoelectric thin film associating with a ternary composite with graphene-embedded PZT:silicone blends, which provides a low-cost skin-like platform for conversion of mechanical motions to electricity and sensing of human activities. This kind of piezoelectric rubber exploits advances in materials, electronics, mechanics, and microfabrication schemes, which serve as the foundations for self-powered, ultrathin (thickness of 1.2 mm), lightweight (67.3 mg cm⁻²), and soft, skin-integrated electronics. The modulus of the best graphene-embedded PZT rubber was measured to be ≈ 1 MPa (Figure S1, Supporting Information). Comparing to the binary piezoelectric (PZT:PDMS) rubbery system, the optimized ternary-based piezoelectric rubber with 0.33% graphene exhibits slightly smaller output voltage but much greater short-circuit current density of 13.23 μ A cm⁻² under foot stepping. Under the guidance of the theoretical calculation, advanced device geometries are experimentally realized, and the corresponding devices allow seamless, conformal integration with skin under extreme deformation and normal daily activities.

2. Results and Discussion

Figure 1a shows schematic illustrations of the soft rubbery piezoelectric-based electronic device. The construction took the form of a multilayer stack that started with a thin soft PDMS (thickness of 0.25 mm, modulus of 70 kPa) as a reversible, soft adhesive substrate and interface to the skin. Flexible metal traces (10 nm Cr/200 nm Au, 200 μ m width) serving as in-plane electrodes for piezoelectric thin films were supported and selectively encapsulated by thin polyimide layers (PI, 2 μ m). The double layers of PI not only acted as electrical encapsulation, but also provided mechanical strain isolation. The exposed area of the metal traces was in direct contact with the piezoelectric layers. Ternary piezoelectric rubbers served as the active elements, which consisted of 81.70 wt% PZT powders (average size of 0.9 μ m), 0.33 wt% graphene, and 17.97 wt% PDMS (thickness of 0.68 mm, Figure 1b; Figure S2, Supporting Information). Another 0.25 mm thick soft silicone (PDMS, 70 kPa) was coated on top as overall encapsulation layer. The fabrication details can be found in the Experimental Section. The overall dimension of the rubbery piezoelectric

based device was 44 \times 27 mm (length \times width) and 1.2 mm of thickness. The majority parts of the electronic device consist of thin, soft silicones or rubbers, which can afford conformal and comfortable mounting onto various regions of the body (Figure S3, Supporting Information). The only high modulus component in this system was the metal electrodes, however, whose stretchability was excellent attributing to the optimized mechanical property (Figure 1c). Figure 1d presents the details of the metal electrode for the piezoelectric rubbers, which used symmetric design of serpentine patterns on both sides of the electrodes for ensuring great stretchability in various directions. After integration the thin piezoelectric rubbers and top PDMS encapsulation layers with the stretchable electrodes, the entire system still maintained excellent flexibility and stretchability, which was soft enough to be mounted on the skin without any irritation (Figure 1e,f).

Figure 1g presents the scanning electron microscopy (SEM) image and the energy-dispersive X-ray spectroscopy (EDX) of the ternary piezoelectric rubbery thin film that consisted of 81.70% of PZT, 17.97% of PDMS, and 0.33 wt% of graphene, where we can observe uniform distributions of lead (Pb), zirconium (Zr), and titanium (Ti) elements over the test area in the piezoelectric rubber film. Figure S4 of the Supporting Information shows more EDX distributions including carbon, oxygen, and silicon elements. The results indicate great uniformity of PZT particles in the rubbery film. The 3D finite element analysis (FEA) guided the design of the metal electrode geometries and entire device layout to achieve a high mechanical performance while minimizing the strain in the Au traces under various skin deformations (see the Supporting Information for details). The simulated strain distribution in the Au traces and corresponding optical images for a representative device mounted on a phantom skin (75 \times 50 \times 5 mm³ soft PDMS with a modulus of 130 kPa similar to that of skin) are shown in Figure 1h,i for stretching, bending and twisting deformations (for additional optical images refer to Figure S5, Supporting Information). To simulate the deformation in the device, the phantom skin was subjected to a set of displacement and rotational boundary conditions corresponding to the specific loading conditions. For stretching, a displacement boundary condition corresponding to 20% stretch was applied to the two ends of the phantom skin, which stretched the device by $\approx 15.2\%$. For bending, a 160° bending angle was applied to the two ends of the phantom skin, which subjected the device to a ≈ 30 mm bending radius. For twisting, the two ends of the phantom skin were subjected to a 90° twisting angle. For all the cases, the maximum principal strains in the Au traces are $\approx 1\%$, significantly less than the fracture strain 5% of Au,^[65] which demonstrates the capabilities of the device to experience large deformation during operation without fracturing.

Figure 2a shows the output electrical signals (open-circuit voltage and short-circuit current) of the soft PZT rubbers associating with different graphene concentrations as a function of various stresses at a constant frequency of 16 Hz. Both the open-circuit voltage and short-circuit current of all the PZT rubbers showed strong dependence on the mechanical stress, where output signals increased with the increase of the stress. Compared to the pure PZT rubbers without any graphene embedding, those graphene-based PZT rubbers showed an

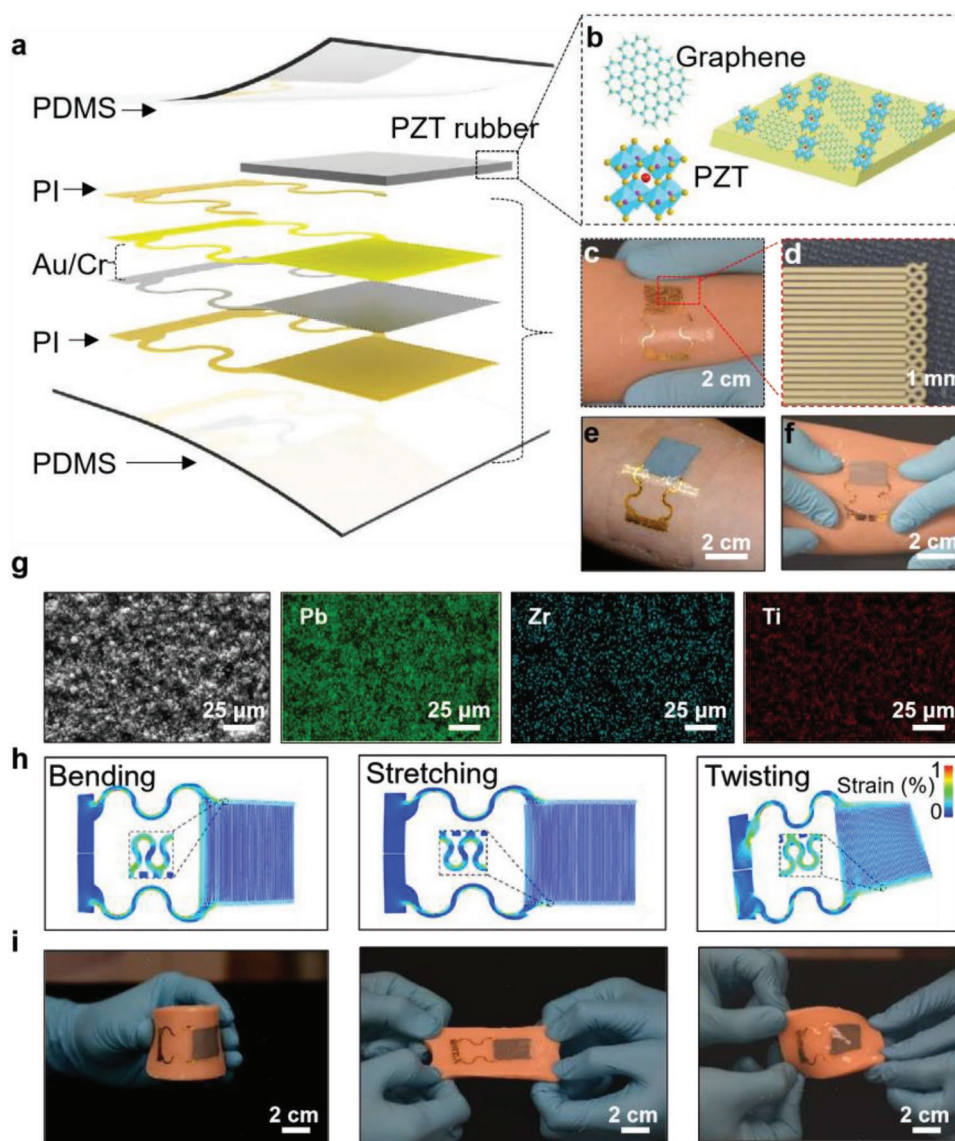


Figure 1. Soft, skin-integrated rubbery electronics with a graphene-embedded PZT/PDMS composite as functional layer. a) Schematic illustration of a skin-like piezoelectric rubbery electronic device. b) Schematic diagram of the ternary piezoelectric rubbers consist of PZT powders, PDMS, and graphene. c) Optical image of the in-plane electrodes for piezoelectric thin films with PI supporting layer and PDMS substrate. d) Enlarged optical image of the electrode pattern. e, f) Optical images of the rubbery piezoelectric electronics attached on the surface of forearm, and deformations together with skin. g) Scanning electron microscope of surface morphology for a PZT/PDMS/0.33 wt% graphene thin film, and the corresponding energy-dispersive X-ray spectroscopy (EDX) images illustrating the distribution of Pb, Zr, and Ti. h, i) FEA results of strain distribution and optical images of the piezoelectric rubbery device under bending, stretching, and twisting.

obvious decrease of the output voltage with the growing weight ratio of graphene at a stress of 20.9 kPa (Figure S6, Supporting Information). However, the output current increased with the increasing graphene contents and achieved a maximum point as the graphene weight ratio of 0.33%, then decreased with further increase of the weight ratio of graphene (Figure S6, Supporting Information). As a result, the output power of the 0.33% graphene-embedded PZT rubbers of 32 nW enhanced ≈ 17 times that of the pure PZT rubbers (1.9 nW). Figure 2b shows the plots of output voltage and current for PZT rubbers with different graphene ratios as functions of frequencies (the input stress is fixed at 20.9 kPa). Similar trends were

observed as the output signal versus stresses, where both the output voltage and current of the graphene embed PZT rubbers increased with the input frequencies, whereas the pure PZT rubbers showed little dependence on the input frequencies. Meanwhile, the trade-off behaviors between current and voltage of the graphene-embedded system could result in significant enhancement of the overall output power.

The results showed that the open-circuit voltage decreased significantly with growing weight fraction of graphene, which was due to the difficulty of poling such piezoelectric rubbers with higher dielectric constants (ϵ_r).^[66] Meanwhile, it is found that the output voltage and current of the composites

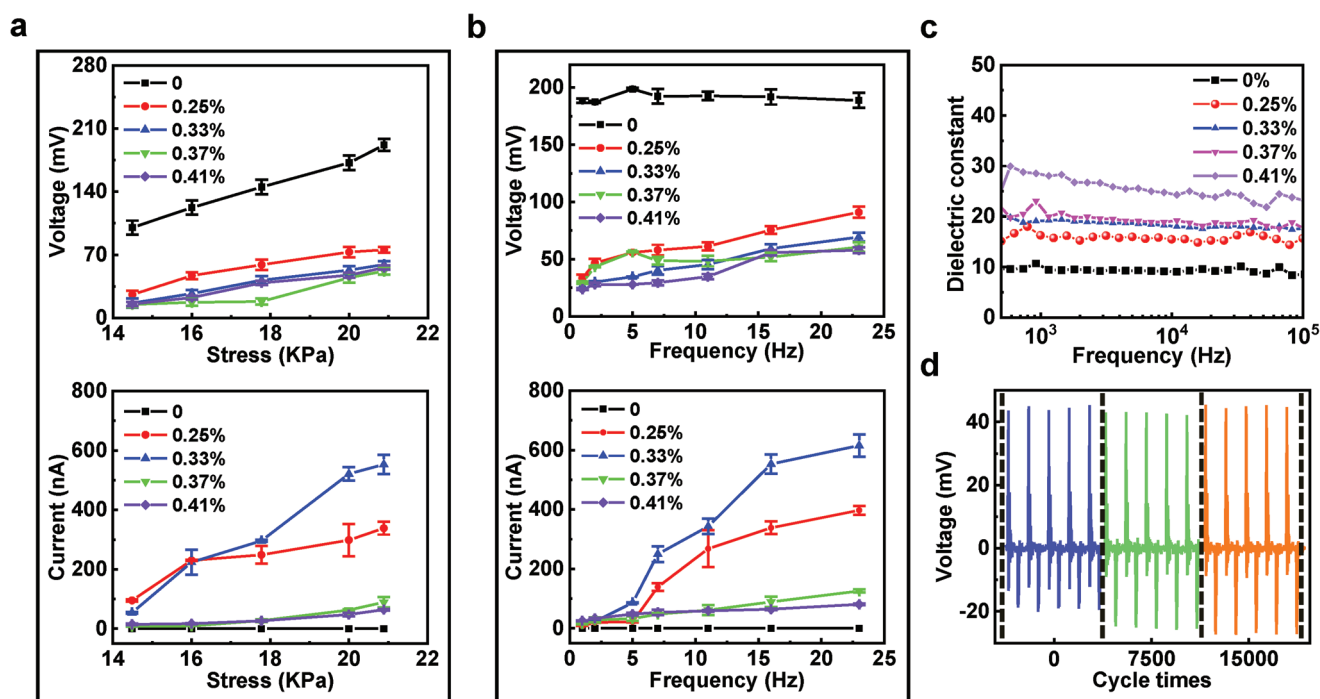


Figure 2. Studies of the electrical properties for the graphene-embedded piezoelectric rubbers. a) Open-circuit voltage, short-circuit current of the piezoelectric rubbers with various graphene weight ratios as function of stress under a constant frequency of 16 Hz, and b) as function of frequency under a constant stress of 20.9 kPa as the contact area is $2 \text{ cm} \times 2 \text{ cm}$. c) Dielectric constant in the frequency range of 3×10^2 to 10^5 of the piezoelectric rubbers with different graphene weight ratios. d) Mechanical durability characterizations of the rubbery device with 15 000 continuous working cycles under the load and frequency of 20 kPa and 10 Hz, respectively.

increased with the increasing of the stress. At the stress of 20.9 kPa with the frequency of 16 Hz, the power output of the device incorporated with 0.33 wt% graphene reached to the highest value (32 nW) with voltage and current of 59 mV and 553 nA, respectively. Dielectric properties of the PZT rubbers with different graphene ratios were measured using an impedance analyzer (Zahner, Germany) in a broad range of frequencies with an AC input (voltage amplitude of 10 mV) at room temperature (Figure 2c), where it can be observed that the ϵ_r increased with the growing ratio of graphene. The results suggested that the ϵ_r enhancement resulted in the output electricity improvement. Graphene is a well-known high conductivity material, which could increase the conductivity of the PZT rubbers and thus lead to a lower the inherent resistance and higher ϵ_r .^[64] However, too low inherent resistance of graphene-embedded composites prevents their poling.^[64,67,68] As a summary, PZT rubbers with 0.33 wt% graphene was proved to be the best rubbery piezoelectric thin films, which was then conducted for a fatigue measurement to investigate the stability. Figure 2d shows the output voltage of the 0.33 wt% graphene-embedded PZT rubbers under 18 000 cycles of 20 kPa mechanical stress loading at a frequency of 10 Hz. No changes in amplitudes observed after thousands of tests proved the great stability and durability of the graphene-embedded PZT rubbers, which indicated the system can be integrated with skin or wearable parts for long-term use. The repeatable and stable electrical output signals in these graphene-embedded PZT rubbers indicate the great uniformity and distribution of the graphene and PZT.

External force applied to the 0.33 wt% graphene-embedded PZT rubbers by finger touching, poking, tapping and fist striking yielded corresponding responses associating with output voltage and current variations (Figure 3a–c). The uniform responses of both current and voltage afforded the skin-integrated devices for accurate sensing external pressure across a broad range from several kPa to MPa. For instance, the measured electrical range (voltage from 0.38 to 3 V, current from 13.5 nA to 1 μA) indicated pressures of touching of ≈ 2.5 kPa, poking of ≈ 12.5 kPa, tapping of ≈ 37.5 kPa, and striking of 0.15 MPa (Figure 3b,c). Here the measurement was conducted based on contact and separation between the finger and the sensor. Moreover, the self-powered nature in the piezoelectric materials allowed the skin-integrated PZT rubbers for energy harvesting from daily body activities. Continuously striking the device by a fist yielded a maximum output power of 3 μW (voltage of 3 V and current of 1 μA), which was sufficient to power many kinds of wearable electronics.^[15,37] Connecting these PZT rubbery devices to rectifier bridges could rectify the voltage for capacitor charging, which demonstrated their capability for energy harvesting and management (Figure S7, Supporting Information). Figure 3d demonstrates the superior sensitivity of the soft PZT rubbers, as the response is very clear to the breath (the examiner blew to the device perpendicularly, the distance is ≈ 9 cm). Four different intensities of breathing, corresponding with flow range from 0.71 standard liter per minute (SPLM) to 7.38 SPLM stimulated the PZT rubbers yielding output voltage from 0.06 to 6.47 mV (Figure 3d). These sensing measurement and results demonstrated the potential

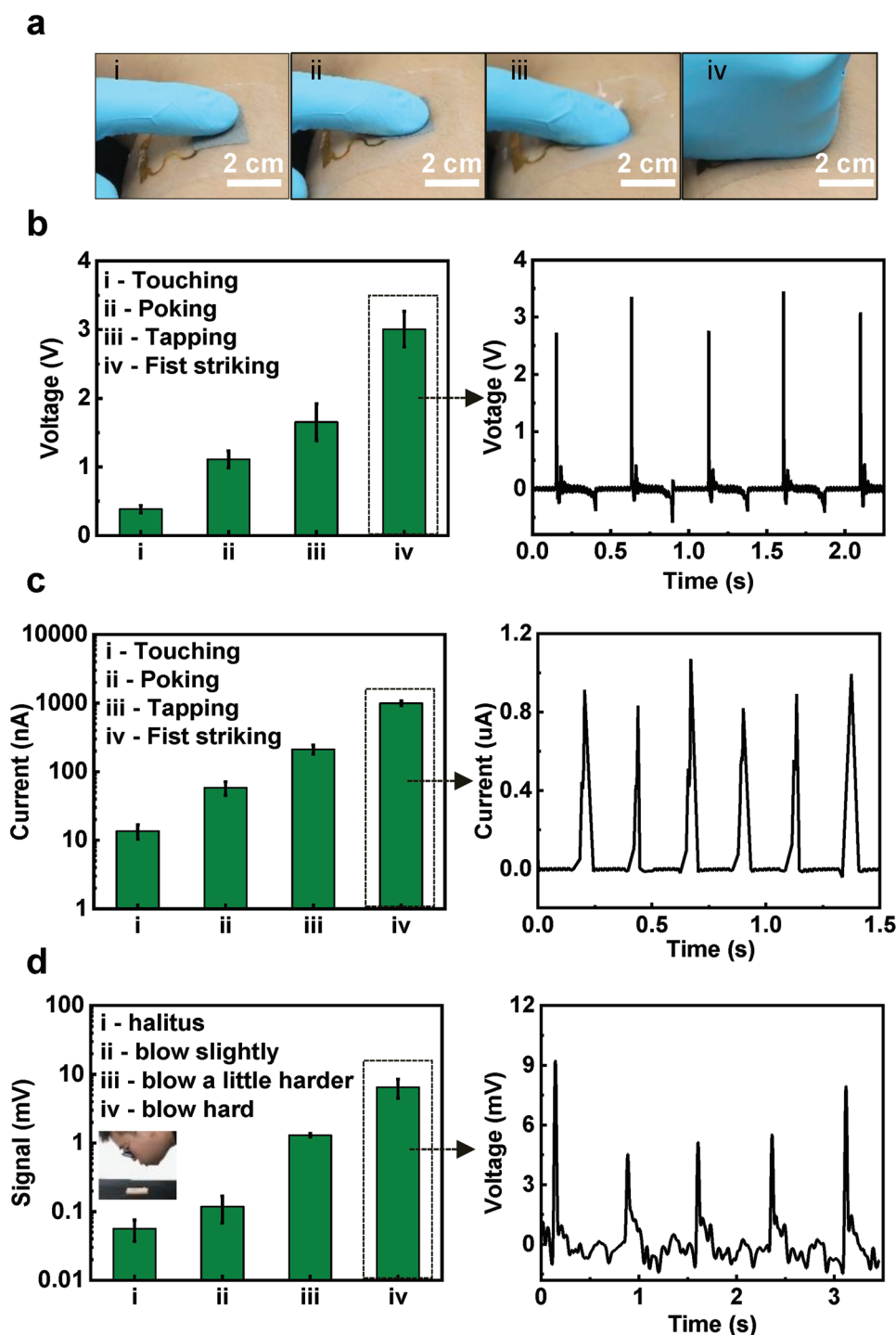


Figure 3. The output signals of the rubbery devices under different external loads. a) Optical images illustrating four different external loads on a representative piezoelectric rubbery device: (i) touching (≈ 2.5 kPa), (ii) poking (≈ 12.5 kPa), (iii) tapping (≈ 37.5 kPa), and (iv) fist striking (0.15 MPa). b,c) Electrical responses in the piezoelectric rubbery devices to four loads, open-circuit voltage (b) and short-circuit current (c) versus loads. d) Open-circuit voltages of the piezoelectric rubbery devices under loads induced by various flows: (i) halitus (0.71 SPLM), (ii) blowing slightly (1.88 SPLM), (iii) blowing a little harder (2.81 SPLM), and (iv) blowing hard (7.38 SPLM).

applications of the soft piezoelectric rubbers in clinically relevant tests and more fields of biomedical engineering.

Large deformations of human bodies typically happen at the joints areas, such as wrists, elbows, and knees, which can afford

greater strains for mechanical energy harvesting. Therefore, wearable devices that can conformally integrate on these joint areas and enhance the power conversion efficiency. **Figure 4a** shows photos of a representative graphene-embedded PZT

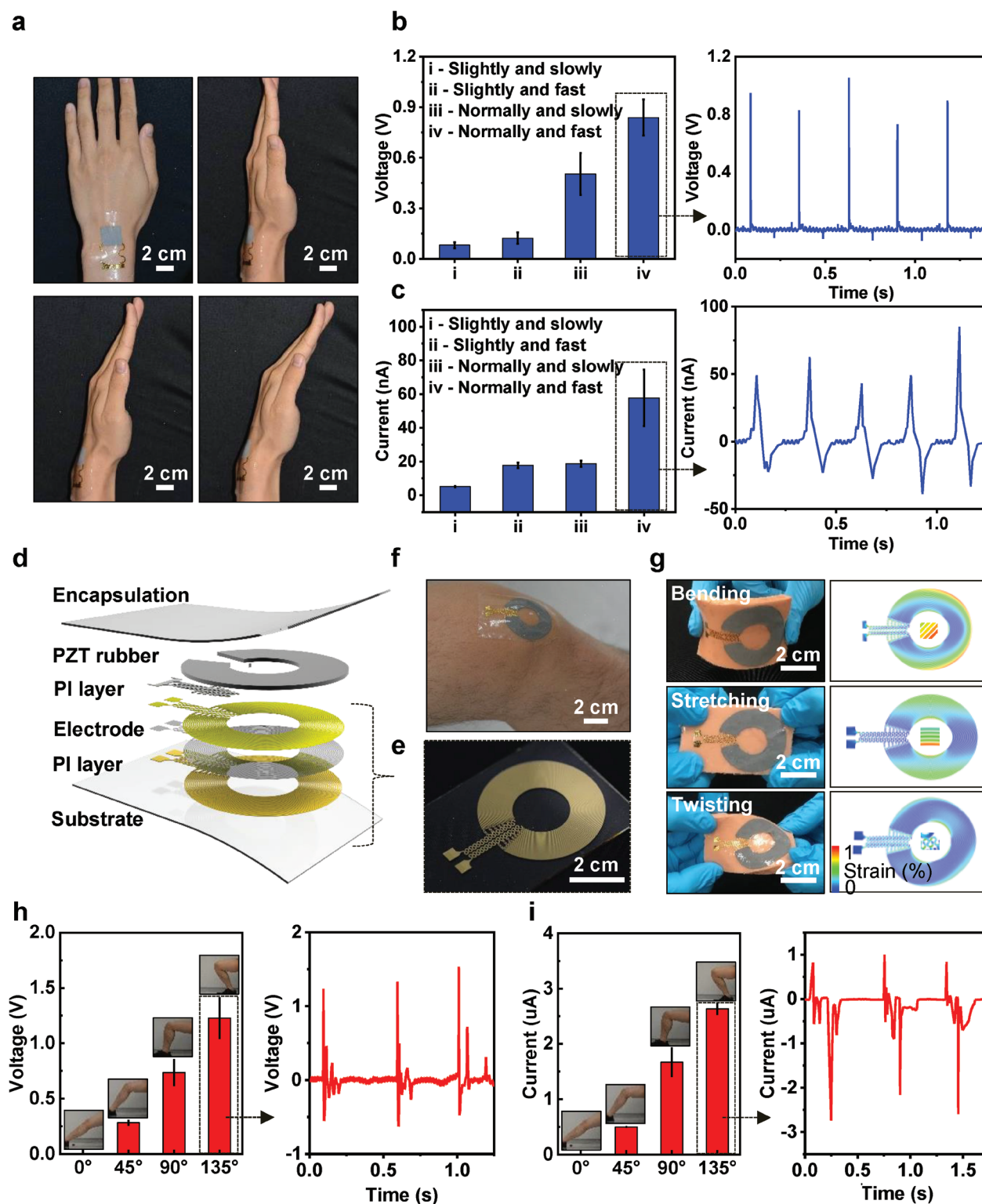


Figure 4. Integration of the piezoelectric rubbery devices on the joints. a) Optical images of a rectangle-shape rubbery device mounted on the wrist, and two motions, including wrist swinging slightly and normally. b,c) Open-circuit voltage and short-circuit current of the piezoelectric rubbery devices under four wrist bending modes, (i) bending slightly and slowly (5°, 1 Hz), (ii) slightly and fast (5°, 4 Hz), (iii) normally and slowly (15°, 1 Hz), and (iv) normally and fast (15°, 4 Hz). d) Schematic illustration of the annulus-shape device. e) Optical image of the annulus-shape electrode pattern. f) Optical image of the annular-shape device mounted on the knee. g) Optical images of the annular-shape device under three mechanical distortions, including bending, stretching, and twisting, and its corresponding FEA results of strain distribution. h,i) Comparison of open-circuit voltage and short-circuit current of the annular-shape device under four external distortions, associating with knee bending of 0°, 45°, 90°, and 135° (the inset images).

rubber device mounted a wrist under different bending angles. Figure 4b,c summarizes the open-circuit voltage and short-circuit current signals of the device under the four different stimuli, (i) bending slightly and slowly (5° , 1 Hz), (ii) slightly and fast (5° , 4 Hz), (iii) normally and slowly (15° , 1 Hz), and (iv) normally and fast (15° , 4 Hz). The output signals showed strong relevance to both frequencies and bending angles, which was consistent with the results shown in Figure 2. A maximum voltage of 0.8 V and current of 58 nA were achieved by the PZT rubbers when the wrist bended at a normal angle and 4 Hz of frequency. It is obvious that the voltage output is more relevance to strain while current output is more sensitive to frequency (Figure 4b,c). These PZT rubbery electronics can also be integrated on some highly pressing relevant locations of the body for collecting energy from large forces, such as stepping by foot. Figure S7 of the Supporting Information shows a PZT rubbery device integrated to a heel of a person (weight, ≈ 80 kg), and thus harvesting energy from daily motions such as walking and running. Due to the high pressure induced by the heel, the PZT rubbery device mounted on the heel yielded an average output voltage and current of 5 V and 52.9 μ A, respectively.

Largely deformed joints (knees and elbows) often provide more mechanical forces, however, the rectangle-shaped PZT rubbery devices cannot guarantee completely conformal lamination due to the unique curvatures of these joints. Combining materials engineering and advanced mechanical designing could overcome this shortcoming. Here, we designed an annulus-shaped PZT rubbery devices with a center hollow layout, which ensured sufficient stress applied on the piezoelectric areas and avoided delamination in the center area at the same time (Figure 4d–f). Figure 4d shows schematic illustration of the annular-shape PZT rubbery device that shares the same layout with the device shown in Figure 1a. However, this geometry adopted an annular-shape along with serpentine interconnects as electrodes (Figure 4e), that avoided stress concentrated on certain areas and provide “empty” area for joints. The design can protect the device from too large deformations (over 90°) caused damage such as the knee bending largely and fast. Computed distributions of strain in the Au traces of the metal electrodes and corresponding optical images of the device on a phantom skin ($75 \times 50 \times 5$ mm³ soft PDMS with a modulus of 130 kPa) in Figure 4g show the results for bending, stretching, and twisting deformations. The device with circular electrodes was modeled in the phantom skin, which was subjected to a set of displacement and rotational boundary conditions corresponding to the loading conditions of the joint areas. For stretching, a displacement boundary condition corresponding to 16% stretch was applied to the two ends of the phantom skin, which stretched the circular device by $\approx 14.2\%$. For bending, a 160° bending angle was applied to the two ends of the phantom skin, which subjected the device to a ≈ 45 mm bending radius. For twisting, the two ends of the phantom skin were subjected to a 70° twisting angle. The maximum principal strains in the Au traces are mainly distributed in the center area for the bending and stretching modes and $\approx 1\%$, significantly less than the fracture strain 5% of Au, which demonstrated the excellent conformal (flexibility and stretchability) and operating capabilities of the device in the joint areas where large deformation was expected. Figure 4h,i present the outputs of the

annulus-shaped PZT rubbery device under three different knee motions (insets of Figure 4h,i), where the maximum open-circuit voltage and short-circuit current were 1.2 V and 2.6 μ A as the knee bends at 135° .

3. Conclusion

In summary, we introduced a thin, soft piezoelectric device capable of laminating on nearly every parts of the body, as a skin-integrated system for energy conversion from mechanical activity to electricity and strain sensing. This platform combined the advances in materials engineering and mechanical designing, provided a new route for realizing self-powered electronic skins. Simply introducing graphene into the PZT, PDMS blend films could effectively enhance the piezoelectric output performance and improve the flexibility, thus significantly lower the fabrication cost simply the processing steps. Experimental and theoretical studies of the piezoelectric rubbery materials and device architectures build foundations and guidelines for the design of skin-like piezoelectric devices. Demonstrations of such devices in pressure sensing in a broad range and energy harvesting from daily body motions indicate potential applications in self-charging wearable electronics, clinical relevance breathing monitoring and others in skin-electronics related areas.

4. Experimental Section

Fabrication of the Piezoelectric Rubbers: As shown in Figure 1b, the ternary piezoelectric rubbers consist of PZT, PDMS, and graphene, where the PZT powder was purchased commercially (diameter of 0.9 μ m on average, Xi'an Yisheng Electronics Co. Ltd., China), PDMS used was Sylgard 184 from Dow Corning Corporation, and graphene powder (average thickness of 1.75 nm; the purity >99 wt%) was purchased from Suzhou Hengzhu Graphite Technology Co., Ltd., China. PZT (10 g), graphene powders (30, 40, 45, and 50 mg), and PDMS (2.2 g, 10:1 weight ratio) were pour into a speed mixer at speed of 500 rpm for 1 h to form rubbery precursors with different blend ratios. Then, the mixtures were transferred into an agate mortar and subsequently grinded for 1 h at room temperature. After fully dispersion, the PZT/PDMS composites with graphene of varying weight ratios were poured into marked beakers for film casting.

Assembly of the Piezoelectric Rubberly Devices: Figure S9 of the Supporting Information shows the assembling process of the device. The fabrication started on a quartz glass, which was first cleaned by acetone, isopropanol and deionized water (DI water) sequentially. A PMMA thin film was spin-coated onto the glass at 2000 rpm (20 mg mL^{-1}) for 30 s and then baked on a hotplate at 200°C for 20 min, which served as the sacrificial layer. A thin layer of PI was spin-coated on the PMMA (poly, amic acid solution 12.0 ± 0.5 wt%, $2 \mu\text{m}$) at 3000 rpm for 30 s, baked at 250°C for 30 min. Next, Au/Cr (200/10 nm) were sputtered onto the PI film, and then patterned by photolithography and etching yielding metal traces in the desired geometries. Here a positive photoresist (PR, AZ 5214, AZ Electronic Materials) was spin-coated at 3000 rpm for 30 s, soft bake on a hot plate at 110°C for 4 min, then exposed to ultraviolet light for 5 s, and finally developed for 15 s in a solution (AZ 300MIF). After development, the PR was removed by acetone and rinsed by DI water. Then, spin casting another layer of PI ($2 \mu\text{m}$ at 3000 rpm for 30 s (annealed at 250°C for 30 min) and then selectively etched by Oxford Plasma-Therm 790 RIE system (patterns defined by photolithography similar as previous step) at the power of 200 W for 10 min, to form encapsulation layers for all the interconnection areas besides the electrodes areas. Immerse the sample, covered by a glass sheet wrapped by dustless cloth, in acetone for 12 h, dissolving the PMMA layer.

Next, water soluble tapes (WSTs) were used to as stamps to pick up the patterns. Exposing the receiving PDMS substrates and the WSTs to UV induced ozone to create chemical groups between the electrodes and PDMS substrates to enhance the bonding strength. Attaching the WSTs on the PDMS and then heated in an oven at 70 °C for 10 min formed strong bonding. Immersing the sample in water to remove the WSTs successfully realized soft stretchable electrodes. Next piezoelectric rubbery precursors were screen-printed onto the stretchable electrodes via screen-printing assisted by a laser cut steel mask (0.68 mm thick, area of 44 × 27 mm). After blade-coating the piezoelectric rubbery precursor, the sample along with the steel mask were heated at 120 °C for 30 min until the PZT rubber completed cured. Finally, the top PDMS encapsulation layer with a thickness of 2 μm was spin-coated and cured.

Characterization: The voltage output data were collected by a PL3516/P Powerlab 16/35 with a constant sampling frequency of 2 × 10⁴ Hz. The current output data were collected by a Keysight B1500A Semiconductor Analyzer. The surface morphology was observed by a scanning electron microscopy (FEI Quanta 450 FESEM). The elastic modulus of PZT/PDMS/0.33 wt% graphene composite was measured using a material testing machine (Lloyd LS1, AMETEK, USA) with an elongation speed of 50 mm min⁻¹ at room temperature. The dimension of the composite is 50 × 10 mm.

FEA: The commercial software ABAQUS (User's Manual V6.10) was used to design the devices and optimize their mechanical performance. The focus of the optimization is to minimize the strain in Au layer when the device undergoes different types of external loads (stretching, bending, and twisting). The PDMS phantom skin and PZT/PDMS/graphene composite were modeled by hexahedron elements (C3D8R) while the thin Au layer and PI films were modeled by composite shell elements (S4R). The number of elements in the model is ≈ 1.2 × 10⁷, and the minimal element size is 1/8th of the width of the narrowest interconnects (200 μm). The mesh convergence of the simulation was guaranteed for all cases. The elastic modulus (*E*) and Poisson's ratio (*ν*) of the materials are *E*_{Au} = 79 GPa, *ν*_{Au} = 0.4, *E*_{PI} = 2.5 GPa, *ν*_{PI} = 0.34, *E*_{skin} = 130 kPa, *ν*_{skin} = 0.49, *E*_{PDMS} = 70 kPa, *ν*_{PDMS} = 0.49, *E*_{composite} = 22 GPa, and *ν*_{composite} = 0.32 for the PZT/PDMS/graphene composite.

The experiments involving human subjects have been performed with the full, informed consent of the volunteers.

Supporting Information

Supporting Information is available from the Wiley Online Library or from the author.

Acknowledgements

Y.L., L.Z., and L.W. contributed equally to this work. This work was supported by City University of Hong Kong (Grant No. 9610423).

Conflict of Interest

The authors declare no conflict of interest.

Keywords

energy harvesting, flexible electronics, PZT, rubbery electronics, skin-integrated electronics

Received: August 29, 2019

Revised: September 26, 2019

Published online: October 14, 2019

- [1] X. Chou, J. Zhu, S. Qian, X. Niu, J. Qian, X. Hou, J. Mu, W. Geng, J. Cho, J. He, C. Xue, *Nano Energy* **2018**, 53, 550.
- [2] L. Chang, Y.-C. Wang, F. Ershad, R. Yang, C. Yu, Y. Fan, *Trends Biotechnol.* **2019**, <https://doi.org/10.1016/j.tibtech.2019.04.001>.
- [3] H. Chen, Y. Song, X. Cheng, H. Zhang, *Nano Energy* **2019**, 56, 252.
- [4] K. Parida, J. Xiong, X. Zhou, P. S. Lee, *Nano Energy* **2019**, 59, 237.
- [5] C. Dagdeviren, P. Joe, O. L. Tuzman, K. Il Park, K. J. Lee, Y. Shi, Y. Huang, J. A. Rogers, *Extreme Mech. Lett.* **2016**, 9, 269.
- [6] S. Huang, Y. Liu, Y. Zhao, Z. Ren, C. F. Guo, *Adv. Funct. Mater.* **2019**, 29, 1805924.
- [7] X. Wang, X. Lu, B. Liu, D. Chen, Y. Tong, G. Shen, *Adv. Mater.* **2014**, 26, 4763.
- [8] D. Ye, Y. Ding, Y. Duan, J. Su, Z. Yin, Y. A. Huang, *Small* **2018**, 14, 1703521.
- [9] X. Yu, T. J. Marks, A. Facchetti, *Nat. Mater.* **2016**, 15, 383.
- [10] H. J. Kim, A. Thukral, C. Yu, *ACS Appl. Mater. Interfaces* **2018**, 10, 5000.
- [11] X. Niu, W. Jia, S. Qian, J. Zhu, J. Zhang, X. Hou, J. Mu, W. Geng, J. Cho, J. He, X. Chou, *ACS Sustainable Chem. Eng.* **2019**, 7, 979.
- [12] H. J. Kim, A. Thukral, S. Sharma, C. Yu, *Adv. Mater. Technol.* **2018**, 3, 1800043.
- [13] H. Liu, J. Zhong, C. Lee, S. W. Lee, L. Lin, *Appl. Phys. Rev.* **2018**, 5, 041306.
- [14] S. Nayak, Y. Li, W. Tay, E. Zamburg, D. Singh, C. Lee, S. J. A. Koh, P. Chia, A. V.-Y. Thean, *Nano Energy* **2019**, 64, 103912.
- [15] J. H. Jung, M. Lee, J. Il Hong, Y. Ding, C. Y. Chen, L. J. Chou, Z. L. Wang, *ACS Nano* **2011**, 5, 10041.
- [16] Z. Lou, S. Chen, L. Wang, K. Jiang, G. Shen, *Nano Energy* **2016**, 23, 7.
- [17] Y. J. Hong, H. Jeong, K. W. Cho, N. Lu, D. H. Kim, *Adv. Funct. Mater.* **2019**, 29, 1808247.
- [18] C. Dagdeviren, B. D. Yang, Y. Su, P. L. Tran, P. Joe, E. Anderson, J. Xia, V. Doraiswamy, B. Dehdashti, X. Feng, B. Lu, R. Poston, Z. Khalpey, R. Ghaffari, Y. Huang, M. J. Slepian, J. A. Rogers, *Proc. Natl. Acad. Sci. USA* **2014**, 111, 1927.
- [19] Q. Shi, T. Wang, C. Lee, *Sci. Rep.* **2016**, 6, 1.
- [20] A. Wang, Z. Liu, M. Hu, C. Wang, X. Zhang, B. Shi, Y. Fan, Y. Cui, Z. Li, K. Ren, *Nano Energy* **2018**, 43, 63.
- [21] Y. A. Huang, Y. Ding, J. Bian, Y. Su, J. Zhou, Y. Duan, Z. Yin, *Nano Energy* **2017**, 40, 432.
- [22] S. Lin, H. Yuk, T. Zhang, G. A. Parada, H. Koo, C. Yu, X. Zhao, *Adv. Mater.* **2016**, 28, 4497.
- [23] Y. Liu, Y. Xu, R. Avila, C. Liu, Z. Xie, L. Wang, X. Yu, *Nanotechnology* **2019**, 30, 414001.
- [24] X. Yu, H. Wang, X. Ning, R. Sun, H. Albadawi, M. Salomao, A. C. Silva, Y. Yu, L. Tian, A. Koh, C. M. Lee, A. Chempakasseril, P. Tian, M. Pharr, J. Yuan, Y. Huang, R. Oklu, J. A. Rogers, *Nat. Biomed. Eng.* **2018**, 2, 165.
- [25] S. Y. Heo, J. Kim, P. Gutruf, A. Banks, P. Wei, R. Pielak, G. Balooch, Y. Shi, H. Araki, D. Rollo, C. Gaede, M. Patel, J. W. Kwak, A. E. Peña-alcántara, K. Lee, Y. Yun, *Sci. Transl. Med.* **2018**, 10, eaau1643.
- [26] S. B. Kim, K. H. Lee, M. S. Raj, B. Lee, J. T. Reeder, J. Koo, A. Hourlier-Fargette, A. J. Bandodkar, S. M. Won, Y. Sekine, J. Choi, Y. Zhang, J. Yoon, B. H. Kim, Y. Yun, S. Lee, J. Shin, J. Kim, R. Ghaffari, J. A. Rogers, *Small* **2018**, 14, 1802876.
- [27] Z. Huo, Y. Peng, Y. Zhang, G. Gao, B. Wan, W. Wu, Z. Yang, X. Wang, C. Pan, *Adv. Mater. Interfaces* **2018**, 5, 1801061.
- [28] J. Jang, B. Oh, S. Jo, S. Park, H. S. An, S. Lee, W. H. Cheong, S. Yoo, J. U. Park, *Adv. Mater. Technol.* **2019**, 4, 1900082.
- [29] J. Xiong, H. Luo, D. Gao, X. Zhou, P. Cui, G. Thangavel, K. Parida, P. S. Lee, *Nano Energy* **2019**, 61, 584.
- [30] A. J. Bandodkar, J. M. You, N. H. Kim, Y. Gu, R. Kumar, A. M. V. Mohan, J. Kurniawan, S. Imani, T. Nakagawa, B. Parish, M. Parthasarathy, P. P. Mercier, S. Xu, J. Wang, *Energy Environ. Sci.* **2017**, 10, 1581.

- [31] C. Dagdeviren, Y. Shi, P. Joe, R. Ghaffari, G. Balooch, K. Usgaonkar, O. Gur, P. L. Tran, J. R. Crosby, M. Meyer, Y. Su, R. C. Webb, A. S. Tedesco, M. J. Slepian, Y. Huang, J. A. Rogers, *Nat. Mater.* **2015**, 14, 728.
- [32] Y. Wang, Y. Qiu, S. K. Ameri, H. Jang, Z. Dai, Y. Huang, N. Lu, *npj Flex. Electron.* **2018**, 2, 6.
- [33] Z. Liu, S. Zhang, Y. M. Jin, H. Ouyang, Y. Zou, X. X. Wang, L. X. Xie, Z. Li, *Semicond. Sci. Technol.* **2017**, 32, 6.
- [34] M. Zhu, Q. Shi, T. He, Z. Yi, Y. Ma, B. Yang, T. Chen, C. Lee, *ACS Nano* **2019**, 13, 1940.
- [35] C. Dagdeviren, S. W. Hwang, Y. Su, S. Kim, H. Cheng, O. Gur, R. Haney, F. G. Omenetto, Y. Huang, J. A. Rogers, *Small* **2013**, 9, 3398.
- [36] Z. H. Lin, Y. Yang, J. M. Wu, Y. Liu, F. Zhang, Z. L. Wang, *J. Phys. Chem. Lett.* **2012**, 3, 3599.
- [37] J. H. Jung, C. Y. Chen, B. K. Yun, N. Lee, Y. Zhou, W. Jo, L. J. Chou, Z. L. Wang, *Nanotechnology* **2012**, 23, 37.
- [38] X. Chen, S. Xu, N. Yao, Y. Shi, *Nano Lett.* **2010**, 10, 2133.
- [39] Y. Yang, S. Wang, Y. Zhang, Z. L. Wang, *Nano Lett.* **2012**, 12, 6408.
- [40] M. Son, H. Jang, M. S. Lee, T. H. Yoon, B. H. Lee, W. Lee, M. H. Ham, *Adv. Mater. Technol.* **2018**, 3, 1700355.
- [41] L. Zhao, Q. Zheng, H. Ouyang, H. Li, L. Yan, B. Shi, Z. Li, *Nano Energy* **2016**, 28, 172.
- [42] J. Wang, H. Wang, N. V. Thakor, C. Lee, *ACS Nano* **2019**, 13, 3589.
- [43] Y. Yang, H. Zhang, Z. H. Lin, Y. S. Zhou, Q. Jing, Y. Su, J. Yang, J. Chen, C. Hu, Z. L. Wang, *ACS Nano* **2013**, 7, 9213.
- [44] Z. Liu, J. Nie, B. Miao, J. Li, Y. Cui, S. Wang, X. Zhang, G. Zhao, Y. Deng, Y. Wu, Z. Li, L. Li, Z. L. Wang, *Adv. Mater.* **2019**, 31, 1807795.
- [45] K. Parida, G. Thangavel, G. Cai, X. Zhou, S. Park, J. Xiong, P. S. Lee, *Nat. Commun.* **2019**, 10, 2158.
- [46] J. Tao, R. Bao, X. Wang, Y. Peng, J. Li, S. Fu, C. Pan, Z. L. Wang, *Adv. Funct. Mater.* **2018**, 1806379.
- [47] P. Vasandani, B. Gattu, J. Wu, Z. H. Mao, W. Jia, M. Sun, *Adv. Mater. Technol.* **2017**, 2, 1700014.
- [48] C. Hou, T. Chen, Y. Li, M. Huang, Q. Shi, H. Liu, L. Sun, C. Lee, *Nano Energy* **2019**, 63, 103871.
- [49] Y. Yang, W. Guo, K. C. Pradel, G. Zhu, Y. Zhou, Y. Zhang, Y. Hu, L. Lin, Z. L. Wang, *Nano Lett.* **2012**, 12, 2833.
- [50] Y. Yang, J. H. Jung, B. K. Yun, F. Zhang, K. C. Pradel, W. Guo, Z. L. Wang, *Adv. Mater.* **2012**, 24, 5357.
- [51] Y. Zi, L. Lin, J. Wang, S. Wang, J. Chen, X. Fan, P. K. Yang, F. Yi, Z. L. Wang, *Adv. Mater.* **2015**, 27, 2340.
- [52] K. Il Park, S. Xu, Y. Liu, G. T. Hwang, S. J. L. Kang, Z. L. Wang, K. J. Lee, *Nano Lett.* **2010**, 10, 4939.
- [53] Y. Duan, Y. Ding, J. Bian, Z. Xu, Z. Yin, Y. Huang, *Polymers* **2017**, 9, 714.
- [54] Y. Lin, H. A. Sodano, *Adv. Funct. Mater.* **2009**, 19, 592.
- [55] E. Bouziane, M. D. Fontana, M. Ayadi, K. Roleder, I. Franke, A. V. Turik, V. Y. Topolov, V. I. Aleshin, *J. Phys.: Condens. Matter* **2001**, 13, 3875.
- [56] S. Xu, Y. Wei, J. Liu, R. Yang, Z. L. Wang, *Nano Lett.* **2008**, 8, 4027.
- [57] G. Schwartz, B. C. K. Tee, J. Mei, A. L. Appleton, D. H. Kim, H. Wang, Z. Bao, *Nat. Commun.* **2013**, 4, 1858.
- [58] L. Tian, B. Zimmerman, A. Akhtar, K. J. Yu, M. Moore, J. Wu, R. J. Larsen, J. W. Lee, J. Li, Y. Liu, B. Metzger, S. Qu, X. Guo, K. E. Mathewson, J. A. Fan, J. Cornman, M. Fatina, Z. Xie, Y. Ma, J. Zhang, Y. Zhang, F. Dolcos, M. Fabiani, G. Gratton, T. Bretl, L. J. Hargrove, P. V. Braun, Y. Huang, J. A. Rogers, **2019**, 3, 194.
- [59] T. Ray, J. Choi, J. Reeder, S. P. Lee, A. J. Aranyosi, R. Ghaffari, J. A. Rogers, *Curr. Opin. Biomed. Eng.* **2019**, 9, 47.
- [60] I. Babu, G. de With, *Compos. Sci. Technol.* **2014**, 91, 91.
- [61] S. Xu, Y. W. Yeh, G. Poirier, M. C. McAlpine, R. A. Register, N. Yao, *Nano Lett.* **2013**, 13, 2393.
- [62] V. Vivekananthan, A. Chandrasekhar, N. R. Alluri, Y. Purusothaman, W. Joong Kim, C. N. Kang, S. J. Kim, *Mater. Lett.* **2019**, 249, 73.
- [63] M. Xia, C. Luo, X. Su, Y. Li, P. Li, J. Hu, G. Li, H. Jiang, W. Zhang, *J. Mater. Sci.: Mater. Electron.* **2019**, 30, 7558.
- [64] I. Babu, G. de With, *Compos. Sci. Technol.* **2014**, 104, 74.
- [65] Y. Zhang, S. Wang, X. Li, J. A. Fan, S. Xu, Y. M. Song, K. J. Choi, W. H. Yeo, W. Lee, S. N. Nazaar, B. Lu, L. Yin, K. C. Hwang, J. A. Rogers, Y. Huang, *Adv. Funct. Mater.* **2014**, 24, 2028.
- [66] P. Fan, L. Wang, J. Yang, F. Chen, M. Zhong, *Nanotechnology* **2012**, 23, 36.
- [67] W. K. Sakamoto, E. de Souza, D. K. Das-Gupta, *Mater. Res.* **2001**, 4, 201.
- [68] H. Gong, Z. Li, Y. Zhang, R. Fan, *J. Eur. Ceram. Soc.* **2009**, 29, 2013.